Geophysical Journal International

Geophys. J. Int. (2024) **239,** 1117–1132
Advance Access publication 2024 September 6
GJI Applied and Marine Geophysics

https://doi.org/10.1093/gji/ggae313

Assessing the effect of offline topography on electrical resistivity measurements: insights from flood embankments

Adrian White [1,2] James Boyd,[1,3] Paul Wilkinson,[1] Holly E. Unwin,[1] James Wookey,[2] John Michael Kendall,[4] Andrew Binley[3] and Jonathan Chambers[1]

[1]*British Geological Survey, Nottingham, United Kingdom. NG*12 5*GG. E-mail: adwh@bgs.ac.uk*
[2]*School of Earth Sciences, University of Bristol, Bristol, United Kingdom, BS*8 1*RJ*
[3]*Lancaster Environment Centre, Lancaster University, Lancaster, United Kingdom, LA*1 4*YQ*
[4]*Department of Earth Sciences, University of Oxford, Oxford, United Kingdom, OX*1 3*AN*

Accepted 2024 August 28. Received 2024 August 20; in original form 2024 April 12

SUMMARY

Electrical resistivity tomography (ERT), a geophysical imaging method, is commonly used on flood embankments (dykes or levees) to characterize their internal structure and look for defects. These surveys often use a single line of electrodes to enable 2-D imaging through the embankment crest, an approach that enables rapid and efficient surveying compared to 3-D surveys. However, offline variations in topography can introduce artefacts into these 2-D images, by affecting the measured resistivity data. Such topographic effects have only been explored on a site-specific basis. If the topographic effects can be assessed for a distribution of embankment geometries (e.g. slope angle and crest width) and resistivity variations, it would allow for targeted correction procedures and improved survey design. To investigate topographic effects on ERT measurements, we forward-modelled embankments with different trapezoidal cross-sections sat atop a flat foundation layer with contrasting resistivity values. Each was compared to a corresponding flat model with the same vertical resistivity distribution. The modelling workflow was designed to minimize the effect of forward modelling errors on the calculation of topographic effect. We ran 1872 unique embankment forward models, representing 144 geometries, each with 13 different resistivity contrasts. Modelling results show that offline topography affects the tested array types (Wenner–Schlumberger, Dipole–Dipole and Multiple–Gradient) in slightly different ways, but the magnitudes are similar, so all are equally suitable for embankment surveys. Three separate mechanisms are found to cause topographic effects. The dominant mechanism is caused by the offline topography confining the electrical current flow, increasing the measured transfer resistance from the embankment model. The two other mechanisms, previously unidentified, decrease the measured transfer resistances from the embankment model compared to a layered half-space but only affect embankments with specific geometries and resistivity distributions. Overall, we found that for typical embankment geometries and resistivity distributions, the resistivity distribution has a greater control on the magnitude of the topographic effect than the exact embankment geometry: the subsurface resistivity distribution cannot be neglected. 2-D inversions are suitable when both the embankment is more resistive than the foundations and when the embankment's cross-sectional area is greater than 4 $m^2\ m^{-2}$ (area scaled to an embankment with a height of 1 m). Topographic corrections, 3-D data acquisition or 3-D forward models are required when these conditions are not met. These are demonstrated using field data from an embankment at Hexham, Northumberland, UK. Improving the accuracy of the resistivity values in ERT models will enable more accurate ground models, better integration of resistivity data with geotechnical data sets, and will improve the translation of resistivity values into geotechnical properties. Such developments will contribute to a better characterized and safer flood defence network.

Key words: Electrical properties; Electrical resistivity tomography (ERT); Numerical modelling; Hydrology.

1 INTRODUCTION

Flood embankments (levees or dykes) are soil or rock earthworks that protect communities and infrastructure from coastal and riverine flooding (Knox *et al.* 2022). Through time, these embankments deteriorate, reducing their level of protection (Simm *et al.* 2012; Tarrant *et al.* 2018; Stirling *et al.* 2021). This deterioration is often initiated internally (Long *et al.* 2006; Tarrant *et al.* 2018) and is particularly associated with local defects (Orlandini *et al.* 2015) at interfaces between materials or in areas with different material properties, such as palaeochannels (Honjo *et al.* 2015). Deterioration can lead to localized failures and millions of dollars of damage (Orlandini *et al.* 2015; Power *et al.* 2021). Detecting areas at risk of failure is, therefore, critically important.

Electrical resistivity tomography (ERT) is a geophysical imaging method that is well suited for detecting deterioration and defects within flood embankments: resistivity varies with lithology, especially clay content (Waxman & Smits 1968; Qi & Wu 2022), as well as with porosity, pore water conductivity, moisture content (Archie 1942; Chambers *et al.* 2014; Jodry *et al.* 2019) and temperature (Hayley *et al.* 2007). ERT is used to spatially or volumetrically characterize the subsurface at multiple scales, from decimetre-scale voids (e.g. Leslie & Heinse 2013; White *et al.* 2023b) to hundred metre wide palaeochannels (e.g. Chambers *et al.* 2012). In addition, it can complement geotechnical testing by informing the extrapolation of discrete geotechnical measurements (Fauchard & Mériaux 2007). For ERT to help detect such defects and classify material properties, we must be confident that the inverted model accurately represents the subsurface.

ERT surveys are often carried out parallel to the long-axis of embankments using linear electrode arrays, sited along the crest or toe due to space and financial constraints (Busato *et al.* 2016; Bièvre *et al.* 2018; Ball *et al.* 2022; You *et al.* 2023). The resulting data sets appear well-suited to processing with 2.5-D inversion methods (referred to as 2-D herein, Sjödahl *et al.* 2006), which have been widely used (e.g. Bièvre *et al.* 2017; Tresoldi *et al.* 2019; Dezert *et al.* 2022). 2-D inversions are quick to run but assume an infinite half-space with no offline changes in resistivity; this includes changes in topography or even water level (Loke *et al.* 2013). Not considering these offline topography and resistivity variations can introduce significant errors into 2-D resistivity models (Sjödahl *et al.* 2006; Fargier *et al.* 2014; Busato *et al.* 2016; Bièvre *et al.* 2018; Hojat *et al.* 2020; Ball *et al.* 2022) as demonstrated with a synthetic model of the embankment at the case study site (Fig. 1; White *et al.* 2023a). 3-D inversions of the 2-D data sets can be used, but are more computationally intensive, require full topographic information of the site and are more underdetermined as there are more model parameters for the same number of measurements, which may result in overly smooth models (Fig. 1, Loke *et al.* 2013; Wilkinson *et al.* 2022).

To correct for topographic effects on 2-D inversions similar to those in Fig. 1, several studies have used a normalization approach (e.g. Fargier *et al.* 2014; Bièvre *et al.* 2018; Hojat *et al.* 2020), where a 3-D model of a specific site is compared to a 1-D or 2-D model with the same vertical resistivity variation, to generate a correction factor. This normalization can either account for just offline topography variations (Marescot *et al.* 2006; Bièvre *et al.* 2018), for topography and pre-defined lithology variations (Fargier *et al.* 2014; Norooz *et al.* 2021; You *et al.* 2023) and for changes in water level (Sjödahl *et al.* 2006; Cho *et al.* 2014; Hojat *et al.* 2020). The calculated correction factor is then applied to actual ERT measurements to correct for offline changes in resistivity and then inverted in 2-D. Hojat *et al.* (2020) found that the effect of topography on an ERT measurement is influenced by the vertical resistivity distribution within the embankment and foundations, explaining the partial correction achieved by Bièvre *et al.* (2018), who corrected just for topography. Fargier *et al.* (2014) demonstrated that for surveys parallel to a flood embankment, those close to changes in slope, i.e. the edge of the crest and embankment toe, are more affected by the embankment topography and contain larger errors.

It is clear that embankment topography can affect ERT measurements, but several key questions remain. (1) What are the key embankment features (e.g. crest width, slope angle, height, area, etc.) that control the magnitude of offline topographic effects? (2) Do different array types have different sensitivities to offline topography? (3) How do variations in subsurface resistivity influence topographic effects on ERT measurements? (4) Is it possible to derive a generic workflow or correction factor to remove the effect of offline topography from ERT surveys? To work to address these questions this paper describes the synthetic forward modelling of a series of trapezoidal embankments with realistic geometries and resistivity contrasts between the embankment fill and foundation strata. The effect of topography on each ERT measurement is assessed by comparing the embankment model with a flat two-layered model with the same vertical resistivity distribution. Systematic forward modelling of a series of embankments with different geometries and resistivity contrasts allows their effect on electrical current flow to be quantified and the mechanisms that cause topographic effects to be understood. Finally, we consider recommendations and best practice guidance for ERT surveys on levees by applying our modelling to an ERT survey of an earth flood embankment in Hexham, Northumberland, England.

2 METHODOLOGY

2.1 Numerical forward modelling

2.1.1 Computation of geometric factors and topographic effects

Electrical resistivity is a fundamental property of every material. It is the ability of a material of a specific size to resist the conduction of electricity through it and is described (for a homogenous material) by:

$$\rho = KR = K \cdot \frac{V}{I}, \tag{1}$$

where ρ is resistivity [Ωm], I electrical current [A], V potential difference [V], K is the geometric factor [m] and R is the transfer resistance [Ω]. The geometric factor allows the resistivity of the material to be calculated in homogeneous materials. For a current flowing uniformly across a sample with a parallel current flow, the geometric factor (K), is,

$$K = \frac{A}{l}, \tag{2}$$

where A is the cross-sectional area of the sample and l is the length over which the potential difference is measured. To measure the resistivity of a material in the ground requires a four-electrode configuration of two current electrodes (A and B) and two potential electrodes (M and N; Fig. 2a). A known current intensity is passed

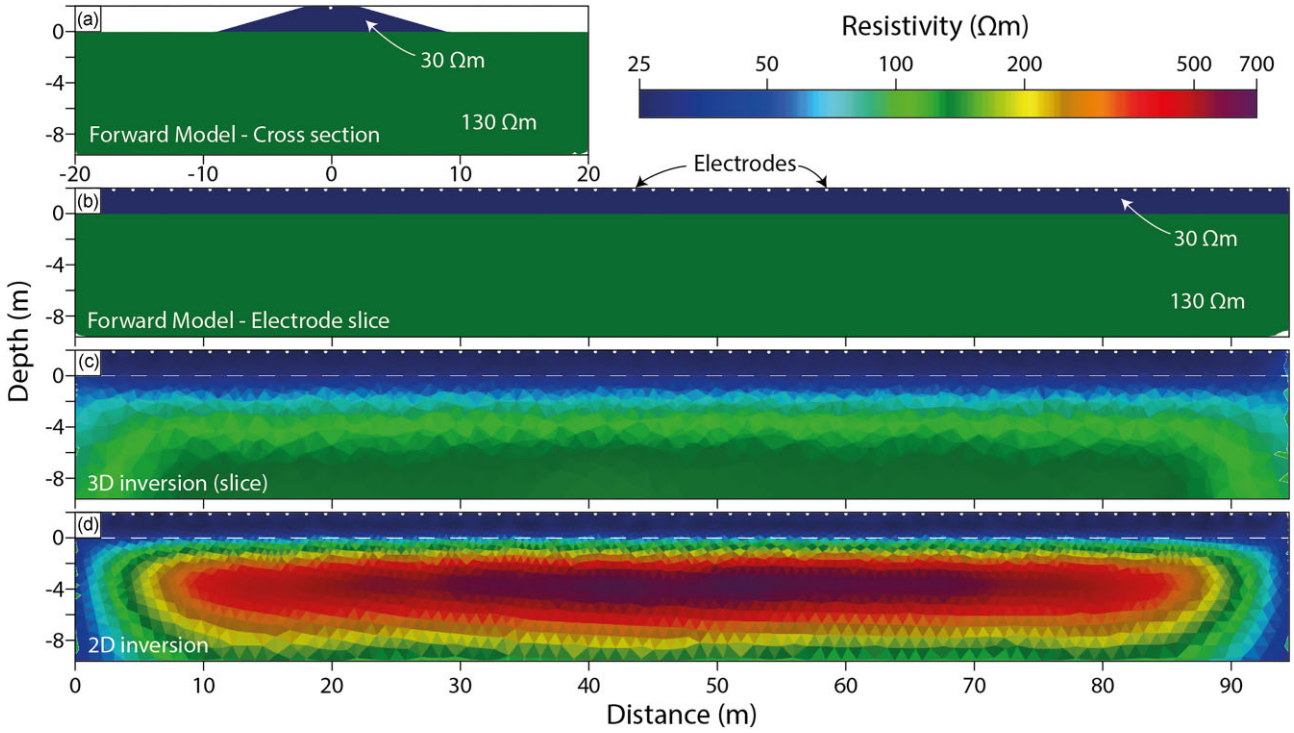

Figure 1. Example of an embankment with a trapezoidal cross section, forward modelled in 3-D in R3t (a, b) and inverted in 3-D with topography (c) and 2-D (d) using software codes R3t and R2, respectively (Binley & Slater 2020). Embankment geometry: height, 2 m; slope, 1:3; crest width, 4 m. The forward model simulated 64 electrodes, 1.5 m apart, for a dipole–dipole array with $a = 1$–3, $n = 1$–8 (Fig. 2a). 2 per cent Gaussian noise was added to the modelled transfer resistances.

between A and B, and the potential difference is measured between M and N; this allows the transfer resistance to be calculated (eq. 1). This can be converted to resistivity by calculating an analytical geometric factor for a four-point measurement assuming each electrode is a point source at the surface of a half-space (Fig. 2a):

$$K = 2\pi\left(\frac{1}{AM} - \frac{1}{BM} - \frac{1}{AN} + \frac{1}{BN}\right)^{-1}. \quad (3)$$

This resistivity value assumes an infinite homogenous half-space (a flat model with a constant resistivity and air above); these assumptions are not fully satisfied for field measurements, so it is called 'apparent resistivity'. For example, a measurement taken along an embankment crest may have a different apparent resistivity compared to the same measurement on an infinite half-space because the electric field is distorted by the embankment sides (Bièvre *et al.* 2018). Horizontal layering within the embankment and foundation layers also affects the electric field, which can alter the topographic effect despite being directly below the survey line (Hojat *et al.* 2020).

To investigate the effect of topography, we compare forward-modelled transfer resistances from an embankment model to a flat model. The flat and embankment models have the same vertical resistivity distribution (two layers) below the line of electrodes (Fig. 2b). In the embankment model, the upper layer forms the trapezoidal embankment, while in the flat model, it is extended laterally to form a two layer half-space. To calculate the difference in the modelled transfer resistances from the embankment model and flat model, we calculate a topographic effect (E):

$$E = \frac{R_{emb}}{R_f}, \quad (4)$$

where R_{emb} and R_f are the measured transfer resistances from the embankment and a flat model, respectively (Hojat *et al.* 2020; You *et al.* 2023). When $E = 1$, there is no topographic effect.

2.1.2 *Model parameter space and meshing*

We need to define a model space comprising realistic parameters to investigate the effect of embankment geometry and subsurface resistivity variation on ERT measurements. The embankment geometries assumed, have trapezoidal cross sections that are typical of those found in North America and Western Europe (e.g. Morris *et al.* 2007; Rickard 2009; CIRIA *et al.* 2013)(Fig. 2b, Table 1). To model resistivity variations, the modelling assumes the embankment is homogenous with a constant resistivity (ρ_1) and the foundation strata is an infinite homogenous half-space with a constant resistivity (ρ_2) (Fig. 3). The range of resistivity values is chosen to reflect materials likely encountered in the field. The embankment materials are often clay and silt rich with resistivity values of ~10–100 Ωm. In contrast, the foundation materials can be much more variable in the range ~1–1000 Ωm, the lowest values represent clays and silts with saline pore waters in coastal environments, while the highest represents dry sand, a typical bedrock or in cold climates permafrost (Reynolds 2011, p. 291; Bièvre *et al.* 2018; You *et al.* 2023). In this modelling, we assume that other variations in resistivity (e.g. an adjacent water course) are negligible in order to focus solely on the embankment effect.

Models with a range of different geometries and resistivity distributions can be created by varying the crest width, height, slope angle, ρ_1 and ρ_2. Two simplifications were made to reduce the number of models that are needed. (i) All embankment geometries were normalized to an embankment height of

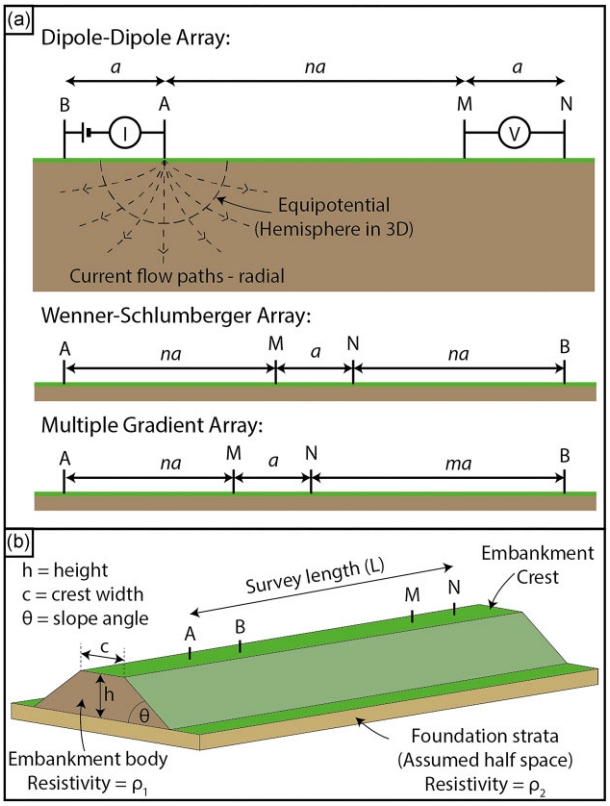

Figure 2. (a) Diagram of array geometry for the Dipole–Dipole, Wenner–Schlumberger and Multiple–Gradient array. A, B = current electrodes. M, N = potential electrodes. a = electrode spacing. n *and* m = positive integers, usually between 1 and 8 for field surveys. A schematic of the current flow is included for a homogenous half-space. (b) The flood embankment geometry assumed in this study includes a homogenous trapezoidal embankment constructed on a homogenous half-space. The electrodes are aligned centrally along the flood embankment crest. © University of Bristol & British Geological Survey © UKRI.

one (Table 1). The range of crest widths and electrode spacings was chosen to allow the model results to be rescaled to embankments of different heights. (ii) The resistivity values of the two layers are characterized by a single resistivity contrast (RC) defined as the ratio of the embankment resistivity to the foundation resistivity, that is ρ_1/ρ_2. The partitioning of electrical current depends only on the resistivity contrast, not the absolute resistivity values (Fargier *et al.* 2014).

The forward modelling considers an array of electrodes located along the middle of the embankment crest. Since we assume that the flood embankment model does not vary along its length, the survey can be simplified and visualized as a 1-D vertical electrical sounding (VES) (Edwards 1977). The range of survey lengths (3–160 m) is based around a dipole–dipole array with dipole lengths, a, of 1–4 electrode spacings and dipole separations, na, where $n = 1$–8 (Fig. 2a), with a range of unit electrode spacings of 1–4 m typically used in embankment surveys (e.g. Niederleithinger *et al.* 2012; Loperte *et al.* 2016; Ball *et al.* 2022). Subsequently, the Wenner, Wenner–Schlumberger and Multiple–Gradient arrays were added, with survey parameters allowing them to span survey lengths of 3–60 m. For each four-electrode measurement, the effective depth was calculated (Edwards 1977). Effective depth (defined here) is the median depth of investigation in a homogenous half-space. This depth varies with the array length and the array geometry. However, the effective depth calculation is only indicative as it does not consider resistivity variations. Still, it is characteristic of the different array properties (e.g. array type, survey length and a and n values) and can be used to compare array types in terms of a single parameter.

The forward modelling uses the finite element method with unstructured tetrahedral meshes, each with between one and two million elements, depending on the exact embankment geometry. The model uses Neumann boundary conditions where the potential gradient normal to the boundary is zero. Each mesh was constructed as a 3-D model using Gmsh (V.4.10.5) and forward modelled using R3t (V.2.01) (Binley & Slater 2020, Fig. 4). To approximate a half-space, the distance from the electrodes to the edge of the model must be sufficiently far so not to significantly affect the modelled transfer resistances (Binley & Slater 2020), ten times the maximum electrode separation satisfied this. To minimize the effect of mesh discretization on the modelled transfer resistances, typically 1–2 per cent of the modelled transfer resistance (Binley & Slater 2020), the finest possible mesh should be used to reduce errors while maintaining sufficiently short run times. Seven cells between adjacent electrode positions were found to be optimal for our models. Additionally, if the same mesh is used for both the flat and embankment meshes, any discretization errors present will cancel out when calculating the topographic effect (eq. 4). To exploit this, our forward modelling workflow derives the embankment mesh from the flat mesh by including the embankment structure in the upper layer (Figs 3 and 4). The cells outside the upper layer's embankment region are removed, creating a new mesh with an updated surface boundary containing only the embankment and foundation layer. This improves on Hojat *et al.* (2020) and Bièvre *et al.* (2018), who both normalize their 3-D models using 2-D models and analytical solutions, respectively. Any discretization errors are retained in their final topographic effect calculation. Additionally, by updating the surface boundary to create the embankment, we do not need to approximate air with near-infinite resistivity values (Hojat *et al.* 2020). We found this approximation insufficient when modelling small differences in transfer resistances.

Table 1. Embankment parameters used to define the model space (Morris *et al.* 2007; Rickard 2009; CIRIA *et al.* 2013)(Fig. 2b), their normalized ranges and sample spacing.

Parameter	Parameter range (units)	Parameter range normalized to height.	Subsampling
Crest width	1–5 (m)	0.16–5 (m/m)	16 samples, equally spaced on a $\log_{10}$ scale
Height	1–6 (m)	1 (m/m)	N/A
Slope angle	1:1–3	1:1–3	9 samples, every 0.25
Resistivity contrast, RC (ρ_1/ρ_2)	0.01–100 (Ωm/Ωm)	0.01–100 (Ωm/Ωm)	13 samples, equally spaced on a $\log_{10}$ scale.
ERT survey length	3–160 (m)	0.5–160 (m/m)	non equal spacing

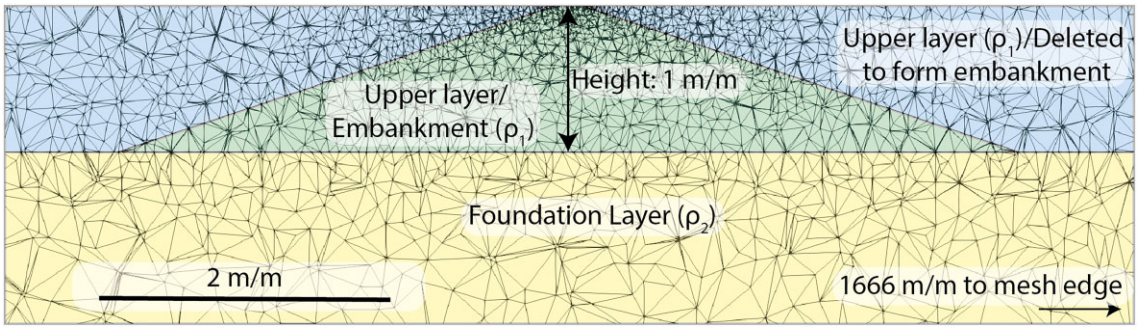

Figure 3. 2-D slice through a forward modelling mesh for the flat model. The blue region is removed to form the embankment model. © University of Bristol & British Geological Survey © UKRI.

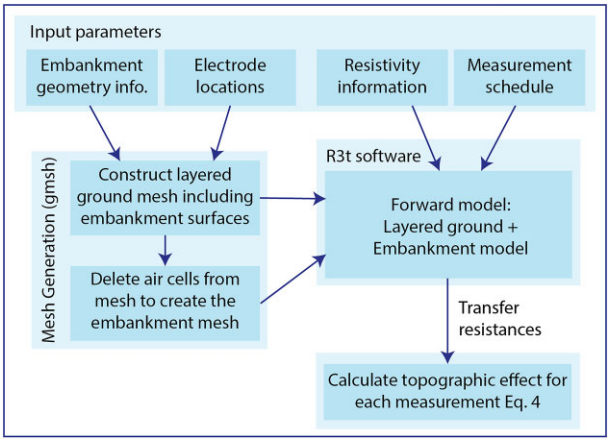

Figure 4. Forward modelling workflow used to calculate topographic effects for different embankment geometries. © University of Bristol & British Geological Survey © UKRI.

It is difficult to assess how discretization errors impact forward-modelled transfer resistances with surface topography and subsurface resistivity variations because direct comparisons to analytical solutions cannot be easily made. However, where direct comparisons with analytical solutions can be made, for example, when the embankment crest width is wide and the electrode spacing is very small, the modelled topographic effect (eq. 4) is within 0.1 per cent of the analytical solution ($E = 1$).

In total, 144 geometries were modelled, with 16 crest widths and nine slope angles. Each geometry was simulated with 13 different resistivity contrasts, totalling 1872 models (Table 1). A corresponding flat model with an identical mesh was run for each embankment model.

3 RESULTS

Here, we consider topographic effects on ERT measurements by comparing each embankment model to its flat model. First, we present the results of a single embankment geometry on different array types and electrode spacings before exploring the effect of different geometries for a homogeneous model, that is RC $= 1$. Finally, we consider how different resistivity contrasts interact with offline topography to affect the resistivity measurements.

3.1 Topographic effect: array type

The effect of the embankment topography on ERT measurements varies for each measurement (Fig. 5). The magnitude of the topographic effect correlates very strongly with the effective depth of the measurement, with all array types having a maximum topographic effect at a very similar effective depth, but array type and geometry also influence it. Broadly, the arrays can be assigned into two groups: those with beta-type adjacent current and voltage electrode pairs (dipole–dipole) and those with alpha-type nested voltage and current electrode pairs (Wenner–Schlumberger and Multiple–Gradient, Fig. 2a). A specific effective depth can be achieved for dipole–dipole and Wenner–Schlumberger arrays by varying the n and a values. For $n = 1$–8, this has a minimal impact on the topographic effect (Fig. 5). In the Multiple–Gradient array, the position of the voltage electrode pair varies between the current electrodes. When the electrode pair is central, it is equivalent to a Wenner–Schlumberger array, so it will have the same topographic effect. Generally, the more asymmetrical the Multiple–Gradient array is, the more its topographic effect diverges from the Wenner–Schlumberger array (Fig. 5).

To simplify the forward modelling results and to allow the mechanisms that cause the topographic effects to be understood, only two fundamental array geometries are presented in the following sections: a Wenner-alpha array (i.e. Wenner–Schlumberger, $n = 1$) and a dipole–dipole array, $n = 1$ (Wenner-beta). The range of a-spacings for these two arrays has been increased to include the full range of array lengths identified in Table 1. The embankment topography fundamentally affects these two arrays differently, so they are investigated separately.

3.2 Topographic effect: homogenous model

The homogenous embankment models (RC $= 1$) show the effect of topography on a sounding curve without considering subsurface resistivity variations (Fig. 6). Cubic splines were fitted through the sounding curves to visually separate them from each other. These splines pass through each data point so do not apply any smoothing. The topographic effects have $E \geq 1$ for the entire depth range of almost every sounding curve. $E > 1$ indicates the transfer resistances returned from the embankment model are higher than those from the corresponding flat model (eq. 4). The topographic effect is small when the effective depth is small and increases with increasing effective depth until a maximum is reached. The topographic effect then decreases with increasing effective depth and tends towards one.

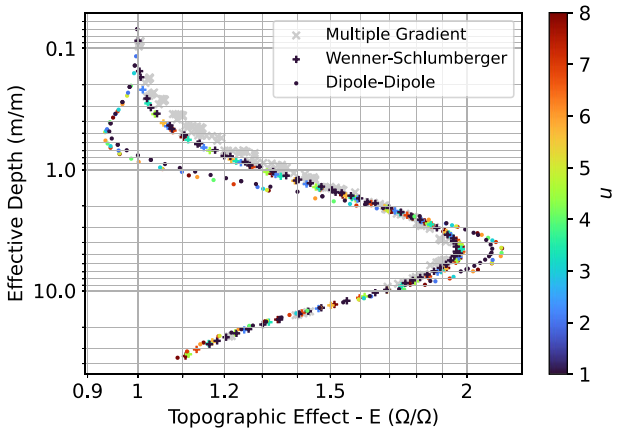

Figure 5. The topographic effect on a sounding curve collected along an embankment crest. The dipole–dipole and Wenner–Schlumberger arrays are coloured by the *n*-value of each measurement. The Multiple–Gradient array is not coloured as it varies with *n* and *m*. Model parameters: Crest width = 2.1 m m^{-1}, Slope angle = 1:3, resistivity contrast (RC) = 0.1. © University of Bristol & British Geological Survey © UKRI.

The crest width and slope angle significantly influence the topographic effect. The topographic effect decreases as the crest width increases, but its peak occurs at increasing effective depths (Figs 6a and b). In contrast, the slope angle changes the magnitude of the peak but only has a limited influence on the effective depth at which it occurs (Figs 6c and d). Array type has little impact on the topographic effect when there is no sub-surface resistivity contrast, with the Wenner and dipole–dipole results having very similar values. The one exception is shown in Fig. 6(d), at an effective depth of ∼0.2 m, $E < 1$ for the dipole–dipole array, while the Wenner array does not. We discuss this below when considering the two layered model.

3.3 Topographic effect: two-layered model

Introducing a resistivity contrast between the embankment and foundation layers can significantly increase or decrease the topographic effect (Fig. 7), for embankment models with identical geometry. When $E < 1$ the modelled transfer resistances from the embankment model are smaller than those from the flat model. These values are surprising as the embankment model is created by removing a relatively conductive region of the model close to the electrode line. Intuitively, we would expect this to always increase the modelled transfer resistances (i.e. $E > 1$).

We have identified three contributions to the topographic effect on resistivity measurements (Fig. 7). (E1) This topographic effect increases the transfer resistances from the embankment model, so $E > 1$, reaching a maximum of 15 (within the model space), but with no theoretical maximum. This effect dominates the homogenous models (Fig. 6) and most of the two-layered models. As RC increases, this effect decreases (Fig. 7). (E2) A relatively small topographic effect superimposed on E1 that decreases transfer resistances from the embankment model, this can result in $E < 1$. E2 peaks at an effective depth of ∼2 m m^{-1} (within the model space) and only starts to have an effect when RC > 1 and the normalized crest width is less than 2 (Figs 7c, d and S1a). The narrower the crest width and the larger the RC, the more pronounced the effect. The slope angle has very little effect, but shallower slopes

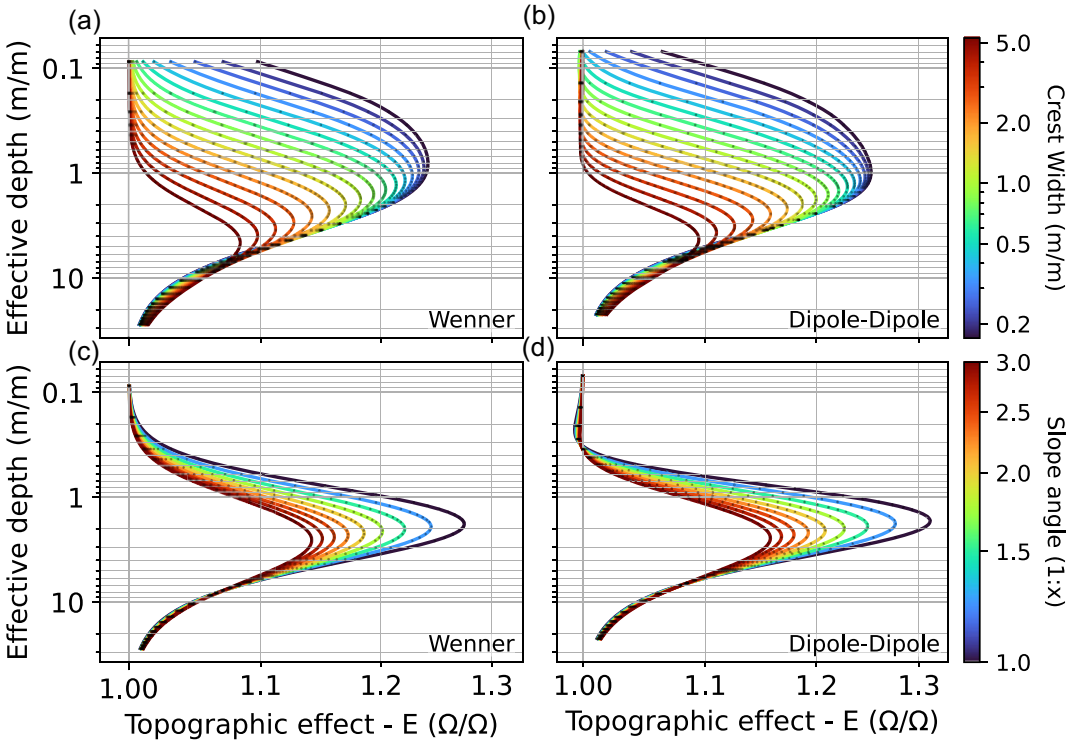

Figure 6. Topographic effect on sounding curves along the embankment crest for a homogenous model (RC = 1). (a) Wenner array for a range of crest widths, constant slope angle of 1:3. (b) Dipole–dipole array for a range of crest widths, constant slope angle of 1:3. (c) Wenner array for a range of slope angles, constant crest width of 2.1 m m^{-1}. (d) Dipole–dipole array for a range of slope angles, constant crest width of 2.1 m m^{-1}. © University of Bristol & British Geological Survey © UKRI.

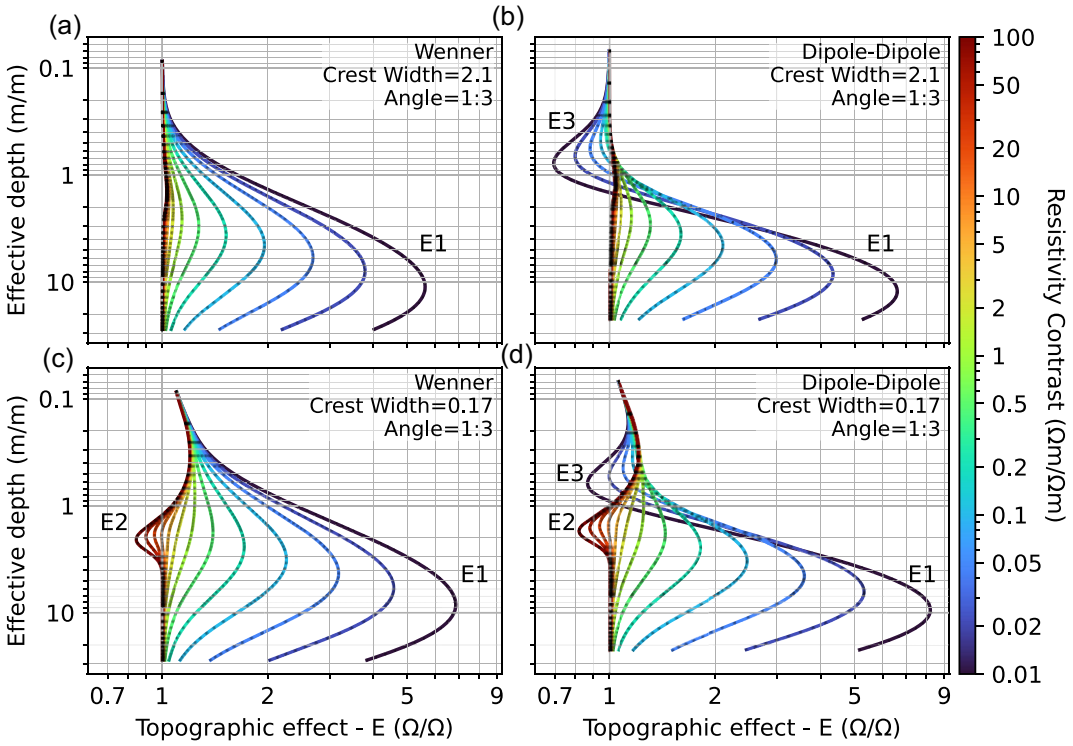

Figure 7. Effect of different resistivity contrasts on Wenner and dipole–dipole sounding curves for two embankment geometries. Panels (a) and (b) have an embankment geometry similar to Fig. 1 and the case study site. Panels (c) and (d) have a very narrow crest width and the same shallow slope angle. Labels E1, E2 and E3 are the three separate contributions to the overall topographic effect.

enhance it slightly (Figs S1a and c). (E3) Similar to E2, it is a relatively small topographic effect superimposed on E1 that decreases transfer resistances from the embankment model; this can result in $E < 1$ (Figs 7b and d). It only impacts dipole–dipole measurements when RC ≤ 1. This is present for all embankment geometries but becomes more pronounced with decreasing RC, two examples are shown in Figs 7(b) and (d). As crest width increases, the magnitude of the effect increases, reaching a maximum at a crest width of $\sim$2.5 m m^{-1} before starting to decrease slightly (Fig. S1b). Steeper embankment slopes marginally increase the effect on E3 (Fig. S1d).

4 CAUSES OF THE TOPOGRAPHIC EFFECTS

The forward modelling shown above reveals that the topographic effect on an ERT measurement depends on interactions between the embankment geometry and resistivity contrast. However, the topographic effect is the product of three separate effects (E1–3), which must be understood to potentially enable topographic effects to be corrected (Fig. 7).

4.1 Effect E1

The topographic effect E1 is the dominant effect on ERT measurement and is responsible for all values of $E > 1$. To understand its origin, consider how the topographic effect changes with effective depth for a homogenous embankment model (Fig. 6). When the effective depth of the resistivity measurement is much smaller than the embankment width, the embankment crest behaves as a homogenous half-space, and there is no topographic effect. As the effective depth increases, the current lines are increasingly distorted in the embankment topography until a peak is reached. At this point, the topography exerts a maximum effect on the resistivity measurement. Combining eqs (1) and (2) shows that smaller cross-sectional areas increase the modelled transfer resistances. In fact, the normalized cross-sectional area of the embankment is an excellent predictor of this peak topographic effect, when RC $= 1$, with a Spearman's rank correlation coefficient of -1.0 (2 s.f., Fig. 8, Gauthier 2001). Further increasing the effective depth means a greater proportion of the current flows in the foundation layer, which is a half-space, reducing the overall topographic effect of the embankment until it is negligible.

Embankment models with smaller crest widths and steeper slope angles are associated with larger topographic effects as both contribute to smaller cross-sectional areas (Fig. 8). The depth of the peak effect again correlates particularly well with the cross sectional area of the embankment (Fig. 8).

Models where RC > 1 have a smaller topographic effect, while when RC < 1 the topographic effect is larger. These differences are the effect of current partitioning between the embankment and foundation layer based on the reciprocal ratio of the resistivity contrast (Telford *et al*. 1990, p. 522):

$$\frac{J_{x_2}}{J_{x_1}} = \frac{\rho_1}{\rho_2} = RC, \tag{5}$$

where J_{x_1} and J_{x_2} are the current densities in the embankment parallel direction for the embankment and foundation layer, respectively. When RC > 1, a greater proportion of the current flows through the foundation layer (Fig. 9a), compared to the homogenous model (Fig. 9b). This reduces the influence of the embankment geometry on the overall current flow and reduces the effect E1. Conversely,

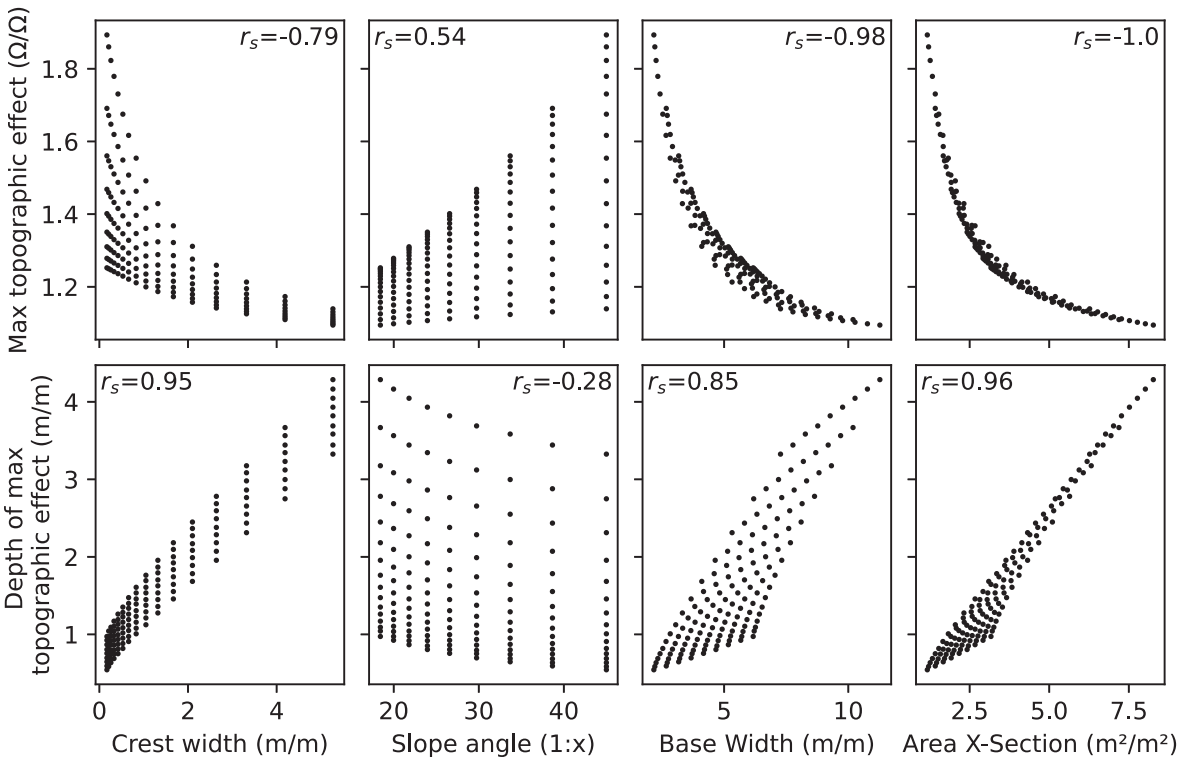

Figure 8. Upper panels: comparison of the maximum topographic effect from each dipole–dipole sounding curve when RC = 1 with the geometrical properties of the embankment. Crest width and slope angle are fundamental, while base width and cross-sectional area are derived. Lower panels: comparison of the effective depth at which the maximum topographic effect occurs to the same geometrical properties. r_s = Spearman's rank correlation coefficient (rounded 2 s.f.).

when RC < 1, the electrical current is channelled in the embankment, increasing the current density (Fig. 9c) and the associated topographic effect (Fig. 7).

4.2 Effect E2

The topographic effect E2 can affect all investigated array types but requires RC > 1 and a narrow embankment crest width that is less than twice the embankment height i.e. crest width < 2 m m^{-1} (Fig. 7, Fig S1A). To visualize the cause of E2, the current density for the embankment model with the largest effect (crest width = 0.17 m m^{-1}, slope = 1:1 and RC = 100 Ωm Ωm^{-1}) was calculated and compared to the flat model (Fig. 10). The two current electrodes are located at 0 and 2 m m^{-1}. A dipole–dipole array with n = 1–5 has effective depths of 0.8–2.9 m m^{-1}, spanning the peak in E2 at ∼2 m m^{-1}, enabling the current density distribution responsible for E2 to be shown (Fig. 10).

The current density distribution in the embankment and flat models is visually similar (Figs 10a and b). Normalizing the embankment model using the flat model highlights differences (Fig. 10c). Close to the current electrodes, the current density is higher in the embankment model (effect E1). This difference decreases along the embankment crest before going through a region where the current density is lower in the embankment model, before returning to a similar current density to the flat model.

The region of relatively low current density forms in response to the narrow embankment geometry and resistivity contrast (RC > 1) partitioning current into the foundation layer (eq. 5). The narrow embankment geometry laterally constrains the electric field, distorting the field lines so pushing the current density contours downwards compared to the flat model (Fig. 10a versus Fig. 10b). This enables the current to flow from the embankment into the foundation layer due to RC > 1 over a shorter horizontal distance than in the flat model, resulting in a region of lower current density and the effect E2 (Fig. 10c). This could occur in larger coastal or estuarine embankments with relatively narrow crest widths compared to their height and low-resistivity foundations containing saline pore water.

4.3 Effect E3

The final topographic effect, E3, impacts only dipole–dipole surveys when RC ≤ 1 (Figs 7b and d). To understand the underlying mechanism, we re-ran one embankment model (crest width = 2.1 m m^{-1}, slope angle = 1:3) and one flat model with RC = 0. This end member was achieved by removing the foundation layer from both the embankment (to leave just the embankment itself) and flat model mesh [to leave a single layer of thickness h = 1 (m m^{-1}), Fig 3]. The modelled transfer resistances are plotted as sounding curves (Fig. 11). For increasing effective depth, embankment transfer resistances from the Wenner array increase, but decrease from the dipole–dipole array. Therefore, for the Wenner array, E > 1 and increases with effective depth (Fig. 11a) while the opposite is true for the dipole–dipole array where E < 1 and becomes increasingly small with depth (Fig. 11b).

To interpret these trends, a comparison is made to three analytical solutions representing three current flow scenarios: 1-D (wire), 2-D (thin conductive sheet) and 3-D (homogenous half-space, Fig. 11, Miccoli *et al.* 2015). The 1-D analytical solution assumes only current flow parallel to the electrodes with a wire-like geometric factor (eq. 2, Fig. 12), where A is the embankment cross-sectional area and

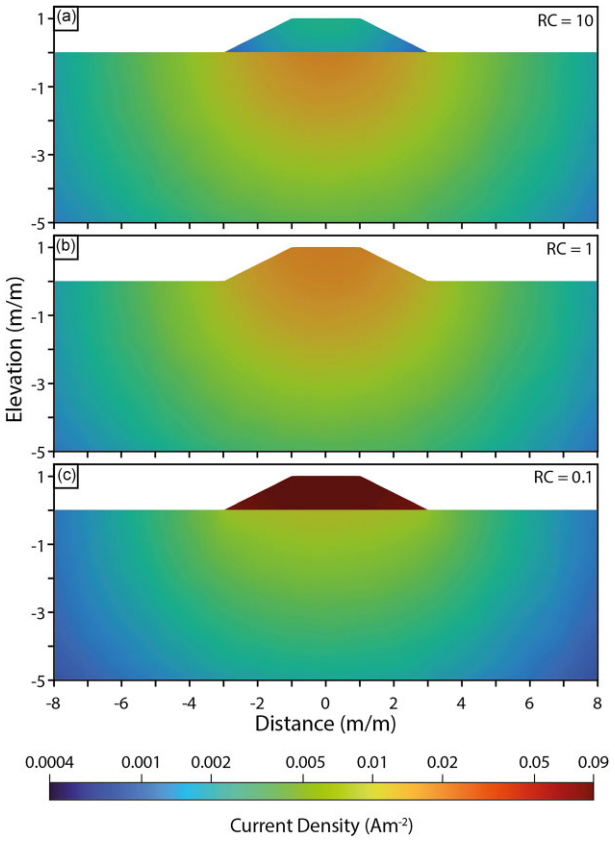

Figure 9. Current density plots showing a cross-section through an embankment (orthogonal to the electrode array) at the midpoint of a Wenner array where $a = 3$ m for three different resistivity contrasts (RC). Embankment geometry crest width: 2 m/m, slope 1:2, height: 1 m/m. A) Embankment = 10 Ωm Foundation 1 Ωm (RC = 10). B) Embankment = 1 Ωm Foundation 1 Ωm (RC = 10). C) Embankment = 1 Ωm Foundation 10 Ωm (RC = 0.1). The colour scale does not resolve the radial current density pattern in the embankment which decreases from 0.09 Am^{-2} to 0.08 Am^{-2} in part C. © University of Bristol & British Geological Survey © UKRI.

l is the distance between the inner pair of electrodes. Considering the current pattern for injecting (or extracting) current from a point on an infinitely long wire, the current splits between both directions (Fig. 12). Using superposition to place current electrodes A and B on the same wire, the current between A and B is the injected current, but outside this, it is always zero. Therefore, the transfer resistances from dipole–dipole will be zero, and cannot be plotted on Fig. 11(b). The 2-D analytical solution assumes current flow in both horizontal planes, the geometric factor is given by (Miccoli *et al.* 2015):

$$K = 2\pi h\left(\ln\left(\frac{BM \cdot AN}{AM \cdot BN}\right)\right)^{-1}, \quad (6)$$

where h is the layer thickness (1 m m^{-1}). The analytical solution assumes that the electrodes extend the full thickness of the layer. The 3-D analytical solution (eq. 3) assumes a homogenous half-space with point electrodes at the surface.

Comparing the modelled transfer resistances to the analytical solutions (Fig. 11) shows that when the effective depth is small, all transfer resistances from the models plot close to the 3-D analytical solution, so approximate homogenous half-spaces. As the effective depth of investigation increases, the transfer resistances diverge from the 3-D analytical solution. The flat models for both

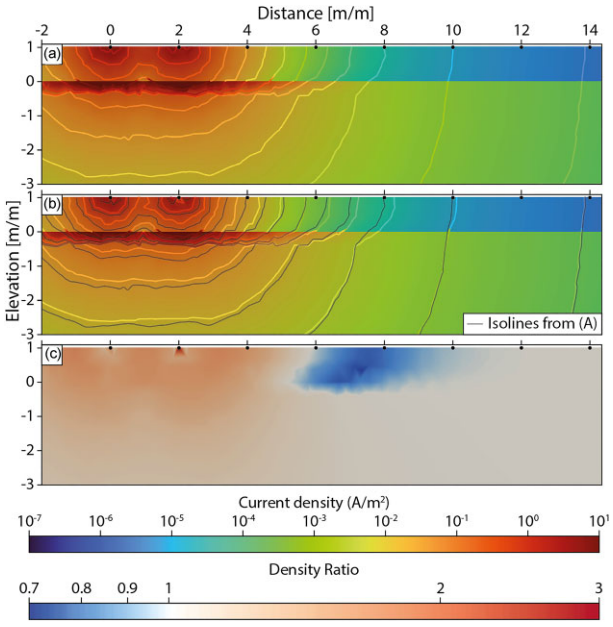

Figure 10. Current density plots of an embankment (a) and equivalent flat (b) model for a pair of current electrodes at 0 and 2 m m^{-1}, visualized by slicing along the line of electrodes. Current density isolines are shown in A and B. The forward model has a resistivity contrast of RC = 100, where the resistivities are 100 Ωm and 1 Ωm for the embankment and foundation layer, respectively. The embankment geometry: crest width = 0.17 [m m^{-1}], slope angle = 1:1. C) The current density ratio (embankment model divided by flat model) © University of Bristol & British Geological Survey © UKRI.

arrays trend to their respective 2-D analytical solution and, therefore, approximate a thin conductive sheet. The embankment models initially appear to behave differently, the Wenner array clearly trends to the 1-D analytical solution, while the dipole–dipole array decreases rapidly to 10^{-8} Ω, beyond which the points scatter, likely due to numerical (discretization) errors within the R3t solution (Fig. 11b). Given the 1-D analytical solution is 0 Ω this is also a trend to the wire like solution.

The comparison of this end member model, RC = 0, to the three analytical solutions demonstrates that the dipole–dipole array has no sensitivity to 1-D current flow. While this end member is very unlikely to exist (embankment sat on plastic geomembrane?), current channelling within the embankment structure is significant enough to cause the effect E3.

5 DISCUSSION

5.1 Importance of the subsurface resistivity distribution

Several recent studies have developed workflows to correct for offline topographic effects (e.g. Bièvre *et al.* 2018) and subsurface resistivity distributions (e.g. Hojat *et al.* 2020), to enable 2-D inversion workflows. Our forward modelling results confirm that both the embankment geometry and the subsurface resistivity distribution influence the topographic effect (Figs 6 and 7). To understand their relative importance, we compare the maximum topographic effect (E1) of the dipole–dipole array to the embankment's normalized cross-sectional area (Fig. 13). This comparison shows that cross-sectional area is an excellent predictor of the maximum topographic effect for a specific RC, but also that the subsurface resistivity distribution has a larger impact on the topographic effect

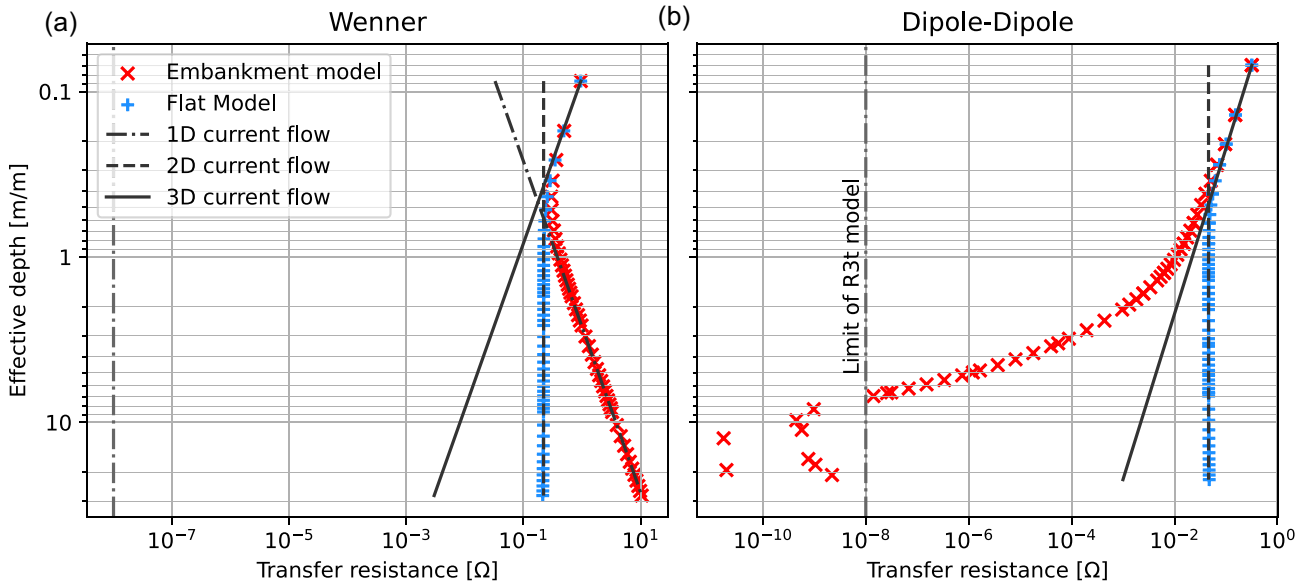

Figure 11. Sounding curves for Wenner (a) and dipole–dipole (b) arrays for an embankment end member and the flat model where RC = 0. Comparison of the modelled transfer resistances is made to 3 analytical solutions that represent 1-D, 2-D and 3-D electric fields. The 1-D analytical solution for dipole–dipole cannot be shown as it is 0 Ω. The embankment resistivity is 1 Ωm, while the lower layer was removed (Fig. 3). 'Limit of R3t model' represents the numerical limit of the R3t forward model, smaller values approximate 0 Ω. © University of Bristol & British Geological Survey © UKRI.

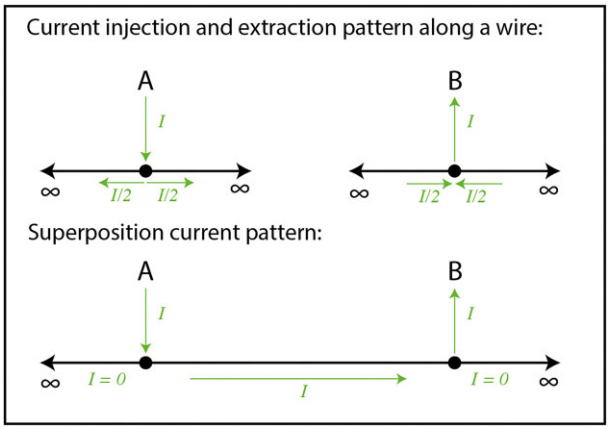

Figure 12. Conceptual model for the 1-D analytical solution, showing the current (***I***) pattern at points A and B if they were each located on an infinitely long wire. Using superposition, the total contributions from A and B can be demonstrated when both are placed on the same wire.

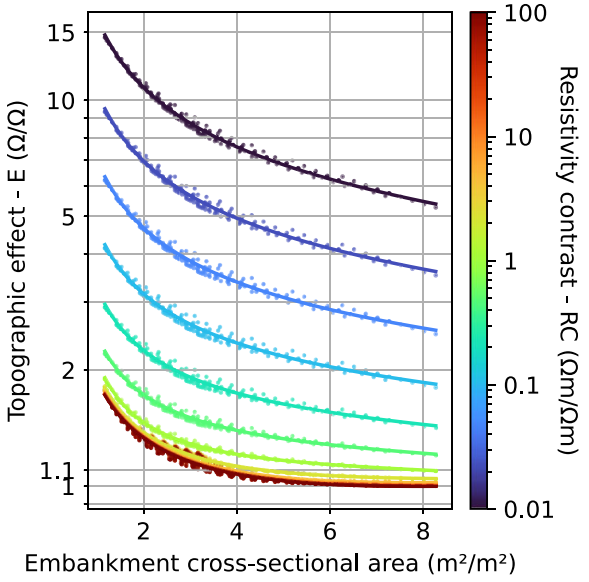

Figure 13. Comparison of the maximum topographic effect for each sounding curve plotted against the normalized cross-sectional area of the embankment. For each RC, a coloured third-order polynomial is fitted through the data to aid visual interpretation. © University of Bristol & British Geological Survey © UKRI.

than the surface topography (within the model space). Therefore, inline changes in resistivity are as, if not more, important as the embankment topography for correcting offline topographic effects. This means that topographic corrections must consider the subsurface resistivity structure, which is often unknown.

5.2 Heterogeneous resistivity distributions

The presented modelling focused on simple two-layer models that assume the embankment and foundations are homogeneous. However, real embankments are unlikely to conform to this ideal. Real embankments can be constructed in layers that may have differing compositions or levels of compaction, be constructed with a clay core surrounded by sand or even a sand core covered in a waterproofing layer of clay (CIRIA *et al.* 2013). Additionally, embankments will have water against them, changing the topographic effect (Hojat *et al.* 2020; Ball *et al.* 2022).

Consider a homogenous embankment model where RC = 1 but with a resistive top layer representing a dry gravel path. The current will preferentially partition from the resistive surface layer into the main embankment structure. This part of the structure is wider than the embankment's crest, so we would expect a slight decrease in effect E1 (Fig. 8). Conversely, for a clay-cored embankment, the current will partition into the core (with resistive material on either

side), which has a steeper geometry than the embankment. We expect this to increase E1 as the normalized cross-sectional area of the core is smaller than the embankment, but it may also increase E3 due to increased current channelling. E2 is unlikely to be present due to the lower resistivity of the core.

If the water level is close to the top of an embankment, the surface geometry, including the water, is substantially changed. The effects E2 and E3 both have geometric controls requiring a narrow embankment and a 'wire-like' embankment that facilitates 1-D current flow, respectively. These are not satisfied with water against the embankment, so E2 and E3 will have no contribution to the topographic effect. Similarly, the effect E1 will be smaller as electrical current can pass through the water adjacent to the embankment, so there is less difference between the current flow paths in the embankment and the flat model. This trend has been observed in previous modelling studies (Cho *et al.* 2014; Hojat *et al.* 2020).

5.3 Recommendations for embankment surveys

2-D inversions are likely sufficiently accurate to allow for the correct identification of lithology when topographic effects are $\lesssim$10 per cent ($E < 1.1$). The 10 per cent threshold is selected for two reasons. (1) A 10 per cent error in apparent resistivity value is unlikely to change the lithological interpretation. (2) It is conservative because there is significant non-linear error propagation from the measured transfer resistances to the inverted model, for example in Fig. 1(d), the 2-D inverted section has errors of 500 per cent, but $E = 1.5$ is the max topographic effect. This error propagation is not explored in this paper; however, a 10 per cent threshold should be sufficiently conservative to enable qualitative interpretations of 2-D inversions. This occurs when $1 \lesssim \mathrm{RC} \lesssim 10$ and the normalized cross-sectional area >4 m^2 m^{-2} (Fig. 13). When RC $\gtrsim$ 10, the topographic effect, E2, starts to become significant, so a 2-D inversion may no longer be appropriate.

Given the importance of the resistivity contrast in determining the topographic effect, it is unlikely to be known if a 2-D inversion is suitable prior to data acquisition. To achieve an accurate resistivity model, 3-D acquisition and inversion is recommended. If only 2-D acquisition is possible, several approaches may improve 2-D inversions. (1) During data acquisition, both a dipole–dipole and Wenner style survey could be acquired along the same line. These array types can have different responses to the embankment topography, so by inverting them together, the model should better account for topography. (2) The 2-D data set can be inverted in 3-D with topography. However, the 3-D inversion is significantly under-constrained (compared to 2-D) and may, for example, return an overly smooth model missing significant true anomalies. (3) Hojat (2024), suggest an iterative approach where the field data is inverted in 2-D and used to inform an increasingly realistic 3-D model of the embankment, however it is unclear if this will converge on the correct resistivity distribution for large resistivity contrasts. Additionally, this time-consuming process would quickly outweigh the time advantage over a 3-D inversion. However, for ERT monitoring, the time saving of a 2-D inversion is multiplied by the number of time steps, which can number in the hundreds or thousands (Tresoldi *et al.* 2019; Boyd *et al.* 2021). Data from the 2-D monitoring array could be corrected using a 3-D model from a one-off 3-D ERT survey (Hojat *et al.* 2020). However, how temporal changes in the resistivity distribution would affect the correction factor would need to be explored.

6 CASE STUDY

To demonstrate the resistivity modelling results, an ERT survey was carried out on a 95 m section of flood embankment located at Warden, Hexham, UK (54.989°N, −2.147°E; Fig. 14a). The embankment is ∼2 m high, with a crest width of 4 m and a slope angle of 1:3, giving a normalized cross-sectional area of 5 m^2 m^{-2} (Fig. 14b). A 1 m resolution digital terrain model collected in March 2019 as part of England's Environment Agency's National LiDAR Program provided the topographic data for the site. It was constructed in 2007 using a homogenous, low-plasticity silty clay with topsoil covering (Fig. 14b). The foundation strata are alluvial deposits of cobles, sands and gravel, as observed in the riverbank, so the resistivity contrast is likely less than 1. Based on a RC <1 and a cross sectional area of 5 m^2 m^{-2} the embankment topography is likely to have a significant impact on the transfer resistance measurements.

6.1 ERT survey

Six ERT survey lines were collected, one along the crest comprising 64 electrodes spaced 1.5 m apart and five lines perpendicular to the embankment, each with 32 electrodes spaced at 1 m intervals (Fig. 14a). An AGI SuperSting R8 resistivity meter was used to make simultaneous potential measurements on up to eight pairs of electrodes. We chose the dipole–dipole array configuration with a = 1–3 and 1–4 (unit spacing) for the crest and perpendicular lines, respectively; and n = 1–8 used for all lines. (Fig. 1a). The dipole–dipole electrode configuration was chosen due to its efficient measurement style on a multichannel instrument, the ease of collecting reciprocal measurements for error modelling and no need for a remote electrode (Dahlin & Zhou 2004).

Data processing and filtering used the open-source software ResIPy (Blanchy *et al.* 2020). Each line was processed to remove all negative apparent resistivities, data with no reciprocal measurement, and measurements with percentage reciprocal errors ≥5 per cent (Tso *et al.* 2017). The percentage reciprocal error (per cent) is calculated by:

$$e_{\%} = \left| \frac{R_f - R_r}{(R_f + R_r)/2} \right| \times 100, \tag{7}$$

where (R_f) and (R_r) are the forward and reverse transfer resistances (Blanchy *et al.* 2020). An error model is fitted for each survey line by fitting a power law error model to the data (Blanchy *et al.* 2020). Finally, the absolute transfer resistance for each reciprocal pair is weighted based on the error model and combined with a 2 per cent modelling error. Of the 3790 reciprocal measurement pairs collected, 145 were removed during data processing and filtering, representing 3.8 per cent of the data.

The data were inverted in ResIPy, a software wrapper for R2 and R3t (Binley & Slater 2020). R2 and R3t use a finite element method for the forward modelling and the inversion is an L_2 smoothness-constrained inversion. Each inversion aimed to converge with a χ^2 of 1.0 within 10 iterations, where χ^2 is a measure of the difference between modelled data and measured data, weighted according to errors (Günther *et al.* 2006; Binley & Slater 2020).

6.2 Survey results

The survey data were inverted in 2-D (Fig. 15a) and 3-D (Fig. 15b) to create two resistivity models of the site. The 2-D inversions converged on average after three iterations with an average χ^2 of 1.04.

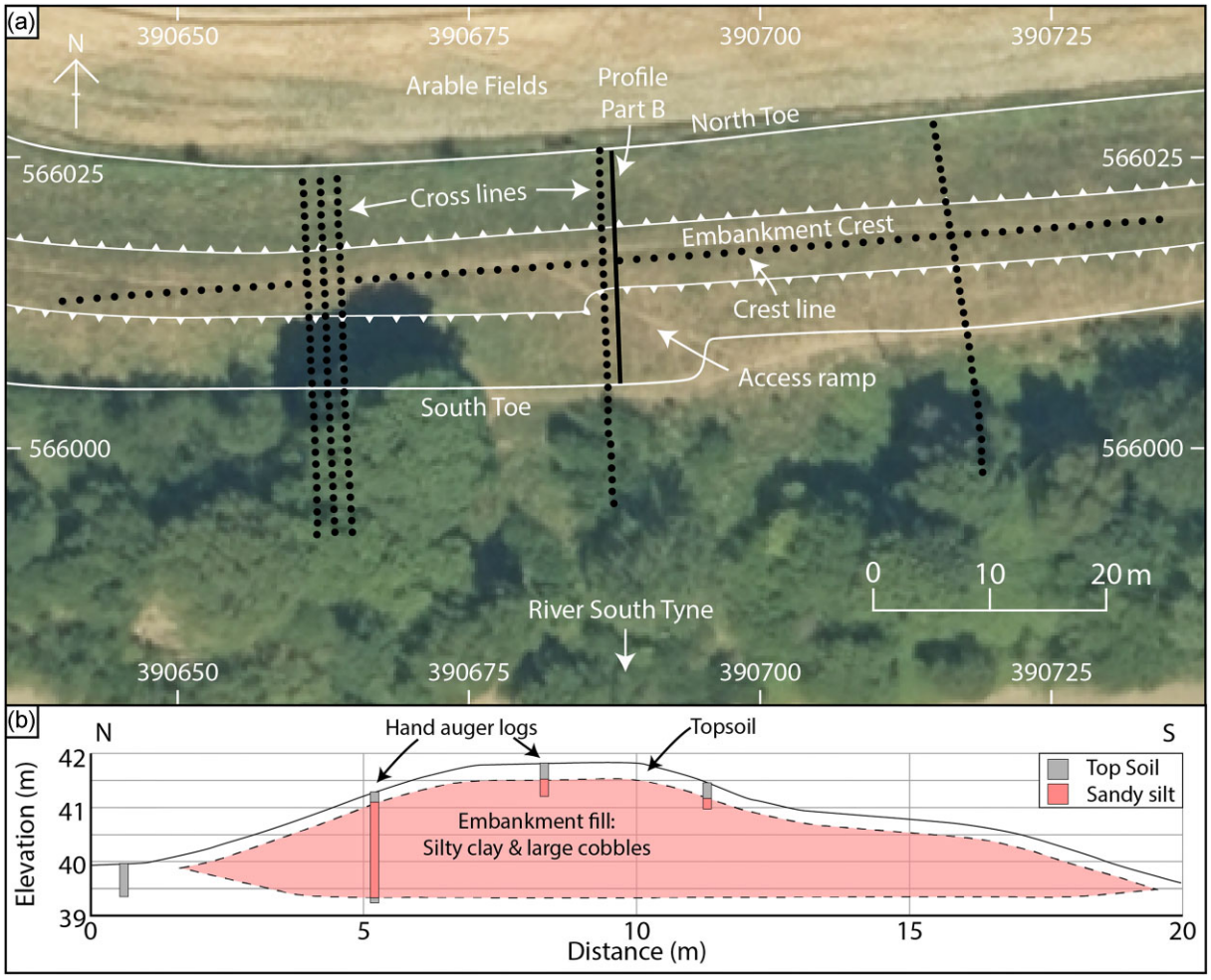

Figure 14. (a) Overview map of field site at Warden, England. The map shows the embankment, location of electrodes and local features for context. (b) Profile across the embankment constructed from LiDAR data and four hand auger holes providing the internal geometry. The cross-section is not representative on the south side as it coincided with a flattened access ramp. Part A base map: High Resolution (25 cm) Vertical Aerial Imagery (2018), 1:500, Tile: ny9066, © Getmapping Plc. © University of Bristol & British Geological Survey © UKRI.

The 3-D inversion converged after two iterations with a χ^2 of 1.39. These models show the site to be characterized by a lower resistivity embankment (*ca*. 30 Ωm) on top of a more resistive foundation layer. There is significant disagreement between the absolute resistivity values within the foundation region. In the 2-D inversions, where the models cross, the resistivity values do not match and there are significant differences between the 2-D and 3-D models (Fig. 15a). This indicates that offline topography is impacting the resistivity data. The 2-D model of the crest line has significantly higher resistivity values up to 900 Ωm, whereas the same line in the 3-D model only returns values where the lines cross up to 240 Ωm and away from the crossing lines 120 Ωm.

6.3 Topographic effect

The topographic effect for the embankment was calculated with the LiDAR-derived topography, assuming a homogenous resistivity for the subsurface (Fig. 16a). There is a range of topographic effects at each effective depth due to variations in topography along the line, such as the access ramp (Fig. 14) and the placement of the line on the crest. Comparing the mean of these topographic effects to the calculated topographic effect for a trapezoidal embankment with approximated dimensions (height = 2 m, crest width = 4 m, slope angle = 1:3 and RC = 1) shows excellent agreement. However, there is an offset at the shallowest effective depths, likely caused by the non-central line placement, which most affects the shallow measurements (Fargier *et al.* 2014) and unevenness in the embankment surface (Fig. 16a).

There is a resistivity contrast between the embankment and foundation layer, with the embankment resistivity of 30 Ωm, and the foundation resistivity of 120–200 Ωm, derived from the 3-D model (Fig. 15B). This gives RC values of 0.25 and 0.15, respectively. Applying the correction factors to the crest line data set and inverting each one in 2-D allows a comparison of the effects (Figs 16b–d). Each correction factor reduces the resistivity values within the foundation layer. To check which one is likely closest to the correct resistivity contrast, the resistivity distribution in the inverted 2-D model should be able to approximate the RC used to correct it. In this case, the RC = 0.25 is the closest fit, indicating the resistivity of the embankment and foundation layer below the embankment have resistivities of about 30 and 120 Ωm, respectively.

Accounting for topographic effects using a simplified geometry and resistivity contrast is effective. However, it relies on accurate knowledge of the embankment geometry and subsurface resistivity distribution with regions of relative homogeneity. In this

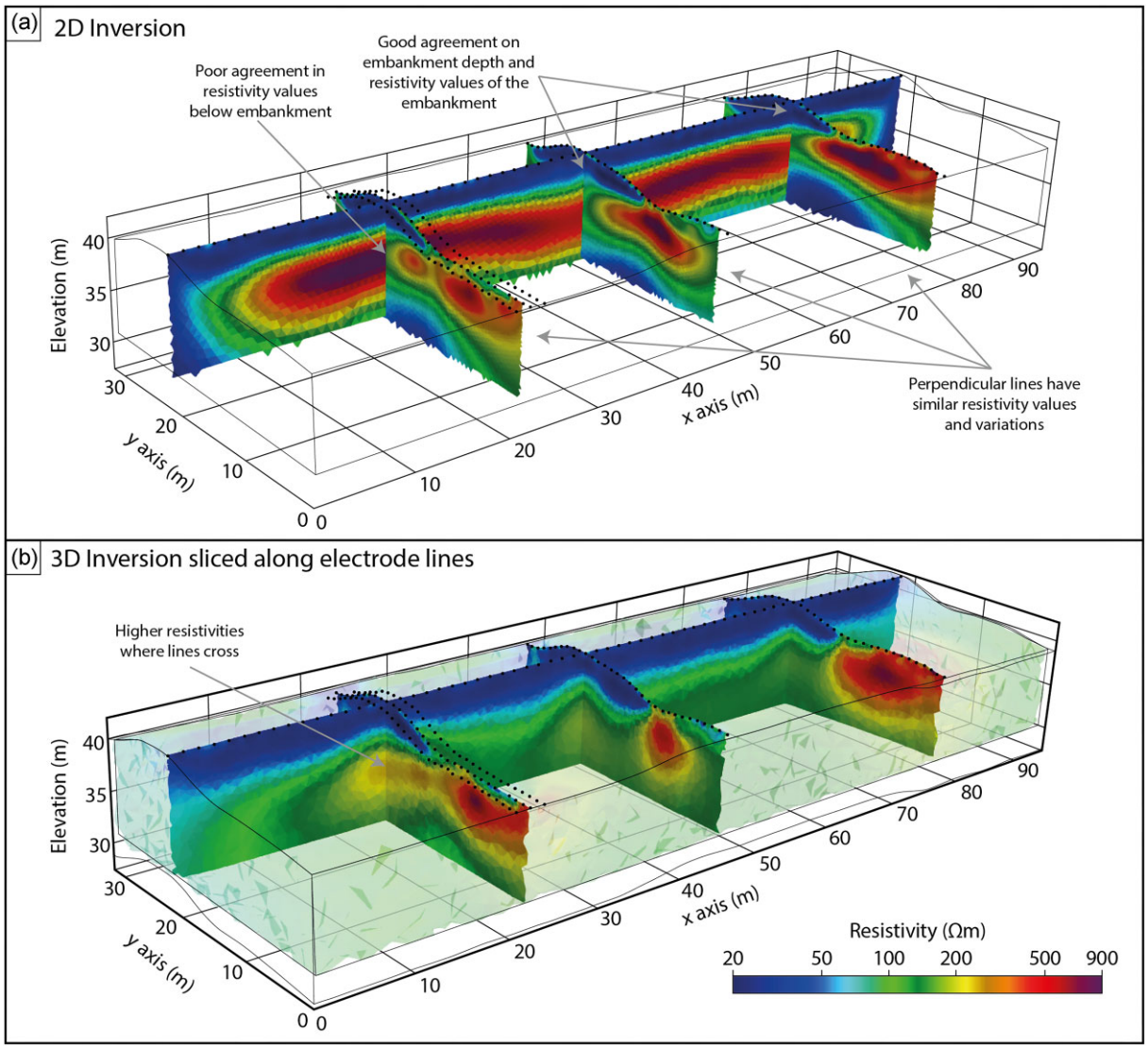

Figure 15. Results of the case study from (a) 2-D inversions of each line and (b) 3-D inversion of the same data set sliced along the lines of electrodes. Both plots have the same resistivity scale. © University of Bristol & British Geological Survey © UKRI.

case, an access ramp up to the embankment crest in the middle of the survey line is not in the trapezoidal model. Not including this probably deepens the low resistivity embankment region between 30 and 60 m. This demonstrates the main issue with trying to account for offline effects: they can only be corrected if they are known about and accurately characterized. Offline subsurface features are only known if there is additional information from other sources or if the ERT survey has used a 3-D acquisition (Jodry *et al.* 2017).

7 CONCLUSION

Through systematic forward modelling of embankment geometries and subsurface resistivity variations, we have explored the impact of offline topography on ERT surveys. The key findings are:

(i) Maximum topographic effects are generally similar in magnitude for all tested array types, but there are key differences between dipole–dipole and Wenner style arrays at certain depths of investigation.

(ii) The array's *n*-value can be neglected as it is almost independent of the topographic effect when the measurement's effective depth is calculated.

(iii) Subsurface resistivity distribution can enhance or suppress the effect of offline topography to such an extent that within the model space, it has a larger control on the topographic effect than the different embankment geometries alone.

(iv) Three separate mechanisms can cause topographic effects. Generally, topographic effects increase the measurement's transfer resistance, but we have shown that transfer resistances can also decrease them for certain embankment geometries and resistivity contrasts.

(v) Dipole–dipole surveys are not sensitive to 1-D wire-like current flow patterns generated by current channelling in the embankment, so they only measure the 3-D component. Wenner arrays are sensitive to both 1-D and 3-D current flow patterns.

To implement these findings into routine embankment surveys the following best practice recommendations are suggested:

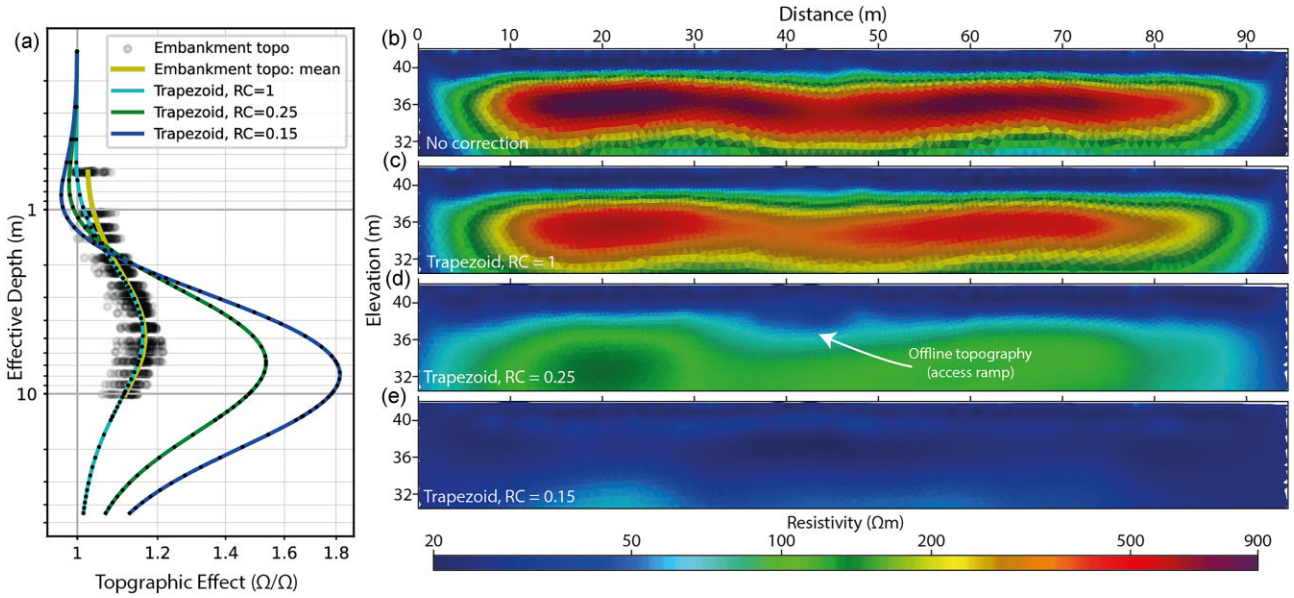

Figure 16. Topographic effect and correction of crest line data from the flood embankment at Warden. (a) Comparison of the topographic effect calculated for each 4-point measurement from LiDAR derived embankment topography to the trapezoidal embankment model with three different resistivity contrasts (RC). (b–e) 2-D Inversion results with different correction factors applied using different resistivity contrasts (RC). © University of Bristol & British Geological Survey © UKRI

(i) 2-D inversions are likely suitable when transfer resistances contain topographic effects of <10 per cent, this is true when the normalized cross-sectional area >4 $m^2\,m^{-2}$ and $1 < RC < 10$, assuming no other internal resistivity variation.

(ii) Where significant topographic effects or complex internal geometries (e.g. clay core) exist, 3-D acquisition and inversion are required to accurately characterize anomalies.

(iii) If only 2-D acquisition is possible for embankments with significant topographic effects, a dipole–dipole and Wenner style survey should be acquired to allow a 3-D inversion to exploit the subtle difference in topographic effect between the two array types.

Further work is needed to better understand how these topographic effects propagate from the transfer resistances to the inverted models, to refine best practice. Where time and resources only allow for 2-D acquisition, using a 3-D inversion shows promise at returning more accurate resistivity values (Fig. 1, e.g. Holmes *et al.* 2022). Further research on optimal mesh design for this under-constrained problem would be valuable. Additionally, 3-D inversions benefit from 3-D data acquisition. Further exploration of novel 3-D arrays, including zig-zag (Robbins & Plattner 2018), parallel (Jodry *et al.* 2017) and crossing (Busato *et al.* 2016) lines, could help develop ERT models that return more accurate resistivity values while balancing acquisition time and cost.

ACKNOWLEDGMENTS

We would like to acknowledge Arnaud Watlet for his assistance with ERT data collection and Dan Normandale (Environment Agency), Mathew Arthur (Environment Agency) and Timothy Grossey (RSK) for supporting this research and the two anonymous reviewers for constructive feedback. This work was funded by a NERC GW4 + UK Doctoral Training Partnership Studentship (Grant NE/L002434/1), the BGS University Funding Initiative (S337) and the ACHILLES project (EP/R034575/1). Adrian White, Paul Wilkinson, Jonathan Chambers, Holly Unwin and James Boyd publish with the permission of the Executive Director, British Geological Survey (UKRI-NERC). All content generated as part of this work is copyright of the British Geological Survey © UKRI 2023/The University of Bristol 2023.

SUPPORTING INFORMATION

Supplementary data are available at *GJIRAS* online.

Supplementary material.docx

Please note: Oxford University Press is not responsible for the content or functionality of any supporting materials supplied by the authors. Any queries (other than missing material) should be directed to the corresponding author for the paper.

DATA AVAILABILITY

The forward modelling code for the different embankment geometries can be downloaded from https://github.com/achw1/ERT-Embankment-modelling. The field data supporting the research is available from Adrian White (adwh@bgs.ac.uk) upon request.

REFERENCES

Archie, G.E., 1942. The electrical resistivity log as an aid in determining some reservoir characteristics, *Trans. AIME,* **146,** 54–62.

Ball, J., Chambers, J., Wilkinson, P. & Binley, A., 2022. Resistivity imaging of river embankments: 3D effects due to varying water levels in tidal rivers, *Near Surf. Geophys.,* **21,** 93–110.

Bièvre, G., Lacroix, P., Oxarango, L., Goutaland, D., Monnot, G. & Fargier, Y., 2017. Integration of geotechnical and geophysical techniques for the characterization of a small earth-filled canal dyke and the localization of water leakage, *J. appl. Geophys.,* **139,** 1–15.

Bièvre, G., Oxarango, L., Günther, T., Goutaland, D. & Massardi, M., 2018. Improvement of 2D ERT measurements conducted along a small earth-filled dyke using 3D topographic data and 3D computation of geometric factors, *J. appl. Geophys.,* **153,** 100–112.

Binley, A. & Slater, L., 2020. *Resistivity and Induced Polarization,* Cambridge Univ. Press.

Blanchy, G., Saneiyan, S., Boyd, J., McLachlan, P. & Binley, A., 2020. ResIPy, an intuitive open source software for complex geoelectrical inversion/modeling, *Comput. Geosci.,* **137,** doi:10.1016/j.cageo.2020.104423.

Boyd, J. *et al.*, 2021. A linked geomorphological and geophysical modelling methodology applied to an active landslide, *Landslides,* **18,** 2689–2704, Landslides.

Busato, L., Boaga, J., Peruzzo, L., Himi, M., Cola, S., Bersan, S. & Cassiani, G., 2016. Combined geophysical surveys for the characterization of a reconstructed river embankment, *Eng. Geol.,* **211,** 74–84.

Chambers, J.E. *et al.*, 2012. Bedrock detection beneath river terrace deposits using three-dimensional electrical resistivity tomography, *Geomorphology,* **177-178,** 17–25.

Chambers, J.E. *et al.*, 2014. 4D electrical resistivity tomography monitoring of soil moisture dynamics in an operational railway embankment, *Near Surf. Geophys.,* **12,** 61–72.

Cho, I.K., Ha, I.S., Kim, K.S., Ahn, H.Y., Lee, S. & Kang, H.J., 2014. 3D effects on 2D resistivity monitoring in earth-fill dams, *Near Surf. Geophys.,* **12,** 73–81.

CIRIA, Ministry of Ecology & USACE, 2013. *The International Levee Handbook,* CIRIA.

Dahlin, T. & Zhou, B., 2004. A numerical comparison of 2D resistivity imaging with 10 electrode arrays, *Geophys. Prospect.,* **52,** 379–398.

Dezert, T., Fargier, Y., Lopes, S.P. & Guihard, V., 2022. Canal dike characterization by means of electrical resistivity, shear wave velocity and particle size data fusion, *J. appl Geophys.,* **204,** dio:10.1016/j.jappgeo.2022.104749.

Edwards, L.S., 1977. A modified pseudosection for resistivity and IP, *Geophysics,* **42,** 1020–1036.

Fargier, Y., Lopes, S.P., Fauchard, C., François, D. & CÔte, P., 2014. DC-electrical resistivity imaging for embankment dike investigation: a 3D extended normalisation approach, *J. appl. Geophys.,* **103,** 245–256.

Fauchard, C. & Mériaux, P., 2007. Geophysical and geotechnical methods for diagnosing flood protection dikes, *Geophysical and Geotechnical Methods for Diagnosing Flood Protection Dikes,* Editions Quae, pp. 124.

Gauthier, T., 2001. Detecting Trends Using Spearman's Rank Correlation Coefficient, *Environ. Forensics,* **2,** 359–362.

Günther, T., Rücker, C. & Spitzer, K., 2006. Three-dimensional modelling and inversion of dc resistivity data incorporating topography—II. Inversion, *Geophys. J. Int.,* **166,** 506–517.

Hayley, K., Bentley, L.R., Gharibi, M. & Nightingale, M., 2007. Low temperature dependence of electrical resistivity: Implications for near surface geophysical monitoring, *Geophys. Res. Lett.,* **34,** 1–5.

Hojat, A., 2024. An iterative 3D correction plus 2D inversion procedure to remove 3D effects from 2D ERT data along embankments, *Sensors,* **24,** doi:10.3390/s24123759.

Hojat, A., Arosio, D., Ivanov, V.I., Loke, M.H., Longoni, L., Papini, M., Tresoldi, G. & Zanzi, L., 2020. Quantifying seasonal 3D effects for a permanent electrical resistivity tomography monitoring system along the embankment of an irrigation canal, *Near Surf. Geophys.,* **18,** 427–443.

Holmes, J. *et al.*, 2022. Application of petrophysical relationships to electrical resistivity models for assessing the stability of a landslide in British Columbia, Canada, *Eng. Geol.,* **301,** doi:10.1016/j.enggeo.2022.106613.

Honjo, Y., Mori, H., Ishihara, M. & Otake, Y., 2015. *On the Inspection of River Levee Safety in Japan by MLIT,* IOS Press.

Jodry, C., Lopes, S.P., Fargier, Y., Côte, P. & Sanchez, M., 2017. A cost-effective 3D electrical resistivity imaging approach applied to dike investigation, *Near Surf. Geophys.,* **15,** 27–41.

Jodry, C., Palma Lopes, S., Fargier, Y., Sanchez, M. & Côte, P., 2019. 2D-ERT monitoring of soil moisture seasonal behaviour in a river levee: a case study, *J. appl. Geophys.,* **167,** 140–151.

Knox, R.L., Morrison, R.R. & Wohl, E.E., 2022. Identification of Artificial Levees in the Contiguous United States, *Water Resour. Res.,* **58,** 1–18.

Leslie, I.N. & Heinse, R., 2013. Characterizing soil-pipe networks with pseudo-three-dimensional resistivity tomography on forested hillslopes with restrictive horizons, *Vadose Zone J.,* **12,** 1–10.

Loke, M.H., Chambers, J.E., Rucker, D.F., Kuras, O. & Wilkinson, P.B., 2013. Recent developments in the direct-current geoelectrical imaging method, *J Appl Geophy,* **95,** 135–156.

Long, G., Mawdesley, M. & Simm, J., 2006. Improved approaches to condition assessment, Vol. 2, Detailed Technical Report, FRMRC UR10, Retrieved from, http://www.floodrisk.org.uk/images/stories/Phase1/UR10Vol2.pdf.

Loperte, A., Soldovieri, F., Palombo, A., Santini, F. & Lapenna, V., 2016. An integrated geophysical approach for water infiltration detection and characterization at Monte Cotugno rock-fill dam (southern Italy), *Eng. Geol.,* **211,** 162–170.

Marescot, L., Rigobert, S., Palma Lopes, S., Lagabrielle, R. & Chapellier, D., 2006. A general approach for DC apparent resistivity evaluation on arbitrarily shaped 3D structures, *J. appl. Geophys.,* **60,** 55–67.

Miccoli, I., Edler, F., Pfnür, H. & Tegenkamp, C., 2015, The 100th anniversary of the four-point probe technique: the role of probe geometries in isotropic and anisotropic systems, *J. Phys. Condens. Matter,* **27,** doi:10.1088/0953-8984/27/22/223201.

Morris, M., Dyer, M. & Smith, P., 2007. *Management of Flood Embankments: A Good Practice Review,* DEFRA.

Niederleithinger, E., Weller, A. & Lewis, R., 2012. Evaluation of geophysical techniques for dike inspection, *J. Environ. Eng. Geophys.,* **17,** 185–195, https://pubs.geoscienceworld.org/jeeg/article-pdf/17/4/185/3015999/185.pdf.

Norooz, R., Olsson, P.I., Dahlin, T., Günther, T. & Bernstone, C., 2021. A geoelectrical pre-study of Älvkarleby test embankment dam: 3D forward modelling and effects of structural constraints on the 3D inversion model of zoned embankment dams, *J. appl. Geophys.,* **191,** doi:10.1016/j.jappgeo.2021.104355.

Orlandini, S., Moretti, G. & Albertson, J.D., 2015. Evidence of an emerging levee failure mechanism causing disastrous floods in Italy, *Water Resour. Res.,* **51,** 7995–8011.

Power, R., Garrett, J., Pettit, A., Waller, S. & Millinship, I., 2021. Modelling the impact of spending on defence maintenance on flood losses, Summary Report, Retrieved from, https://www.abi.org.uk/globalassets/files/publications/public/flooding/modelling-the-impact-of-spending-on-defence-maintenance.pdf

Qi, Y. & Wu, Y., 2022. Electrical conductivity of clayey rocks and soils: a non-linear model, *Geophys. Res. Lett.,* **49,** doi:10.1029/2021GL097408.

Reynolds, J.M., 2011. *An Introduction to Applied and Environmental Geophysics,* John Wiley & Sons.

Rickard, C.E., 2009. Floodwalls and flood embankments, in *Fluvial Design Guide,* TU Delft Research Repository.

Robbins, A.R. & Plattner, A., 2018. Offset-electrode profile acquisition strategy for electrical resistivity tomography, *J. Appl. Geophys.,* **151,** 66–72.

Simm, J. *et al.*, 2012. The significance of failure modes in the design and management of levees—a perspective from the International Levee Handbook team, in *Comprehensive Flood Risk Management,* 1st edn, pp. 1–15, eds, Klijn, F. & Schweckendiek, T., CRC Press.

Sjödahl, P., Dahlin, T. & Zhou, B., 2006. 2.5D resistivity modeling of embankment dams to assess influence from geometry and material properties, *Geophysics,* **71,** G107–G114.

Stirling, R.A., Toll, D.G., Glendinning, S., Helm, P.R., Yildiz, A., Hughes, P.N. & Asquith, J.D., 2021. Weather-driven deterioration processes affecting the performance of embankment slopes, *Géotechnique,* **71,** 957–969.

Tarrant, O., Hambidge, C., Hollingsworth, C., Normandale, D. & Burdett, S., 2018. Identifying the signs of weakness, deterioration, and damage

to flood defence infrastructure from remotely sensed data and mapped information, *J. Flood Risk Manag.,* **11,** 317–330.

Telford, W.M., Geldart, L.P. & Sheriff, R.E., 1990. *Applied Geophysics*. 2nd edn. Cambridge: Cambridge University Press.

Tresoldi, G., Arosio, D., Hojat, A., Longoni, L., Papini, M. & Zanzi, L., 2019. Long-term hydrogeophysical monitoring of the internal conditions of river levees, *Eng. Geol.,* **259,** 1–11.

Tso, C.H.M. *et al.*, 2017. Improved characterisation and modelling of measurement errors in electrical resistivity tomography (ERT) surveys, *J Appl Geophy,* **146,** 103–119.

Waxman, M.H. & Smits, L.J.M., 1968. Electrical conductivities in oil-bearing shaly sands, *Soc. Pet. Eng. J.,* **8,** 107–122.

White, A., Watlet, A., Blake, A., Wilkinson, P., Dashwood, B. & Chambers, J., 2023a. Multi-scale characterisation of a clay flood embankment, Warden, Northumberland, in *Proceedings of the NSG2023 29th European Meeting of Environmental and Engineering Geophysics,* 3-7 September 2023, Edinburgh, United Kingdom, pp. 1–5.

White, A., Wilkinson, P., Boyd, J., Wookey, J., Kendall, J.M., Binley, A., Grossey, T. & Chambers, J., 2023b. Combined electrical resistivity tomography and ground penetrating radar to map Eurasian badger (Meles Meles) burrows in clay-rich flood embankments (levees), *Eng. Geol.,* **323,** doi:10.1016/j.enggeo.2023.107198.

Wilkinson, P.B. *et al.*, 2022. Windowed 4D inversion for near real-time geoelectrical monitoring applications, *Front. Earth Sci. (Lausanne),* **10,** doi:10.3389/feart.2022.983603.

You, Y., Pan, X., Fu, W., Wang, Y., Yu, Q., Guo, L. & Wang, X., 2023. Topographical effect of high embankments on resistivity investigation of the underlying permafrost table, *Permafr Periglac Process,* **35,** 24–32.